Coherent diffractive photoproduction of ρ^0 mesons on gold nuclei at RHIC

STAR Collaboration

Abstract

The STAR Collaboration reports on the photoproduction of $\pi^+\pi^-$ pairs in gold-gold collisions at a center of mass energy of 200 GeV/nucleon. These pairs are produced when a nearly-real photon emitted by one ion scatters from the other. The differential cross section $d\sigma/dt$ clearly exhibits a diffraction pattern, compatible with scattering from a gold nucleus, with 2 dips visible. We fit the $\pi^+\pi^-$ mass spectrum to a combination of ρ^0 and ω resonances, plus a direct $\pi^+\pi^-$ continuum; the ratio of ρ^0 : direct $\pi^+\pi^-$ is consistent with previous measurements in lighter systems. The ω component is comparable with that expected from the measured ω photoproduction cross section and $\omega \to \pi^+\pi^-$ branching ratio.

Keywords: Rho photo-production, diffraction, hadronic form factor
PACS: 25.75.Dw, 25.20.Lj, 13.60.-r

1. Introduction

Relativistic heavy ions are accompanied by high fluxes of nearly-real photons, due to their large electric charge and the strongly Lorentz contracted electric fields. In relativistic heavy ion collisions, these fields can produce photonuclear interactions. When they collide and interact hadronically , the strong interactions obscure these electromagnetic interactions. However, when they physically miss each other, the photonuclear interactions can be visible; these are refered to as Ultra-Peripheral Collisions (UPCs). The photon flux is well described within the Weizsäcker-Williams formalism [1, 2]. These exchanged photons are nearly real, with virtuality ($\langle Q^2\rangle \sim 2 \times 10^{-3}\text{GeV}^2$).

For photoproduction of ρ mesons at RHIC near mid-rapidity, the photon-nucleon center of mass energy ranges from from 9 to 18 GeV, depending on the final state transverse momentum and rapidity. In this region, the ρ^0 photoproduction cross section increases slowly with energy; the $\gamma p \to \rho p$ cross section is well described by the soft-Pomeron model [3]. The Pomeron itself may be described as a gluon ladder [4, 5].

A more detailed model considers the photon as a combination of Fock states: a bare photon with virtual $q\bar{q}$ pairs, plus higher virtual states. It was succesful at describing many of the Deep Inelastic Scattering (DIS) measurements performed at HERA [6] and is also applicable in the UPC environment.

Many models have been proposed to describe the ρ photoproduction cross section in ultra-peripheral heavy ion collisions. The first calculation used HERA data on $\gamma p \rightarrow \rho p$ as input to a classical Glauber calculation to predict the cross section with heavy ions [7]; it successfully predicted the ρ photoproduction cross section at RHIC energies from 62 GeV/nucleon [8] to 130 [9] and 200 GeV/nucleon [10], and up to 2.76 TeV/nucleon at the LHC [11]. A later calculation used a dipole model, treating the $q\overline{q}$ pair as a dipole, plus a quantum Glauber calculation, which found a cross section about 50% lower, in disagreement with the data [12]. Most recently, a modification of the quantum Glauber calculation has been proposed; in this model nuclear shadowing reduces the calculated ρ cross section to match the data [13]. Other calculations which include nuclear saturation mechanisms, including the colored glass condensate [14, 15]. Two-photon production of $\pi^+\pi^-$ pairs, but the cross-section is much smaller than for photonuclear interactions [16].

Because of the high photon flux these UPC events have a high probability to be accompanied by additional photon exchanges that excite one or both of the ions, into a Giant Dipole Resonances (GDR) or higher excitation. The GDRs typically decay by emitting a single neutron, while higher resonances usually decay by emitting two or more neutrons [17]. These neutrons have small momentum with respect to their parent ion, so largely retain the beam rapidity. For heavy nuclei, the total cross section for multi-photon interactions nearly factorizes [18] , with the combined cross section given by an integral over impact parameter space: $\sigma(A_1A_2 \rightarrow A_1^*A_2^*\rho) = \int d^2b P_{0\mathrm{Had}}(b) P_1(A^*) P_2(A^*) P(\rho)$, where $P_{0\mathrm{Had}}(b)$, $P_1(A^*)$, $P_2(A^*)$ and $P(\rho)$ are the respective probabilities for not having a hadronic interaction, exciting the two ions and producing a ρ. Each photon-mediated reaction occurs via independent photon exchange, so all four probabilities are tied together only through a common impact parameter [19]. The individual photon-mediated subreactions have a strong impact parameter dependence, so the combined probability is highest for impact parameters $b >\approx 2R_A$, where R_A is the nuclear radius.

2. Experimental setup and Analysis

This letter reports on the measurement of exclusive ρ and ω meson and direct $\pi^+\pi^-$ photo-production in UPCs between gold ions using the Solenoidal tracker at RHIC (STAR) detector at a center of mass energy of 200 GeV/nucleon, using data recorded during Run 10. The current data sample is about 100 times larger than in previous measurements [10] at this energy. The improved statistics allow for much higher precision studies, leading to two main new results. The first is the observation of a detailed diffraction pattern, clearly showing the first and second dips, with a possible third. This diffraction pattern can be used to determine the distribution of the hadronic matter in gold nuclei. Second, the high-statistics $\pi\pi$ invariant mass distribution cannot be fit with just ρ and direct $\pi\pi$ components; an additional contribution from photoproduction of ω, with $\omega \rightarrow \pi^+\pi^-$ is required for an acceptable fit.

Five STAR components were used for triggering and event reconstruction in the analysis: the Time Projection Chamber (TPC), Time of Flight system (TOF), Beam Beam Counters (BBCs) and East and West Zero Degree Calorimeters (ZDCs).

The STAR TPC [20] efficiently detects charged tracks with pseudo-rapidities $|\eta| < 1.5$, using 45 layers of pad rows in a 2 m long cylinder. In the 0.5 T solenoidal magnetic field, the momentum resolution is $\Delta p/p = 0.005 + 0.004p$ with p in GeV/c. The TPC can also identify charged particles by their specific ionization energy loss (dE/dx) in the TPC. The dE/dx resolution is 8% for a track that crosses 40 pad rows. This gives good pion/kaon/proton separation up to their respective rest masses.

The other detector components were used solely for triggering. The TOF system that surrounds the TPC in azimuth, with coverage in pseudo-rapidity $|\eta| < 1$. At higher rapidities, charged particles are detected using the two BBCs, one on each side of the nominal interaction point. Each is formed with 18 scintillator tiles arranged around the beam pipe, covering a pseudo-rapidity window of $2 < |\eta| < 5$ [21]. The ZDCs are small hadron calorimeters installed downstream of the collision region to detect neutrons at beam rapidity [22].

The trigger selected events with small multiplicity in the central detector, along with one or more neutrons in each ZDC, along the lines described in [10]. It requires low activity in the TOF detector (at least two and no more than six hits), no charged particles detected in the BBC detectors and finally, showers in both ZDC detectors corresponding to at least the equivalent of one neutron with beam momentum or up to four beam momentum neutrons. The threshold on each ZDC calorimeter was set at 50 ADC channels (the centroid of the one neutron peak sits at 198 channels) making them fully efficient. The integrated trigger luminosity was 1074 $(\mu b)^{-1}$ ($\pm 10\%$); a total of 38 million triggers were recorded.

The analysis selected events containing a pair of tracks with opposite charges (like-sign pairs were used as a background measure) that were consistent with originating from a single vertex, located within 50 cm longitudinally of the center of the interaction region. The tracks were required to have at least 14 hits in the TPC (out of a possible 45), and have dE/dx values within 3σ of the expected dE/dx for a pion with that trajectory. Both tracks in each pair were required to have a valid hit in the TOF system; this cut rejected events from other beam crossings. It also limited the track acceptance largely to the region $|\eta| < 1.0$. The 384,000 events with a $\pi^+\pi^-$ pair mass in the range $0.25 < M_{\pi\pi} < 1.5$ GeV were saved for further evalutation. This included photoproduced ρ and ω decays to $\pi^+\pi^-$ as well as directly photoproduced $\pi^+\pi^-$ pairs.

The largest backgrounds for this analysis were low-multiplicity hadronic interactions (peripheral ion-ion collisions), whith some of their charged particles out of the TPC acceptance. Other backgrounds come from other UPC reactions or from cosmic-rays accompanied by in-time mutual Coulomb exitation. Pure electromagnetic production of e^+e^- pairs contribute less than 4% to the ρ peak [9]. The decay $\omega \to \pi^+\pi^-\pi^0$ produces a $\pi^+\pi^-$ pair below the ρ^0 peak, but with a larger p_T than for coherent production; it contributes a few percent (2.7% in

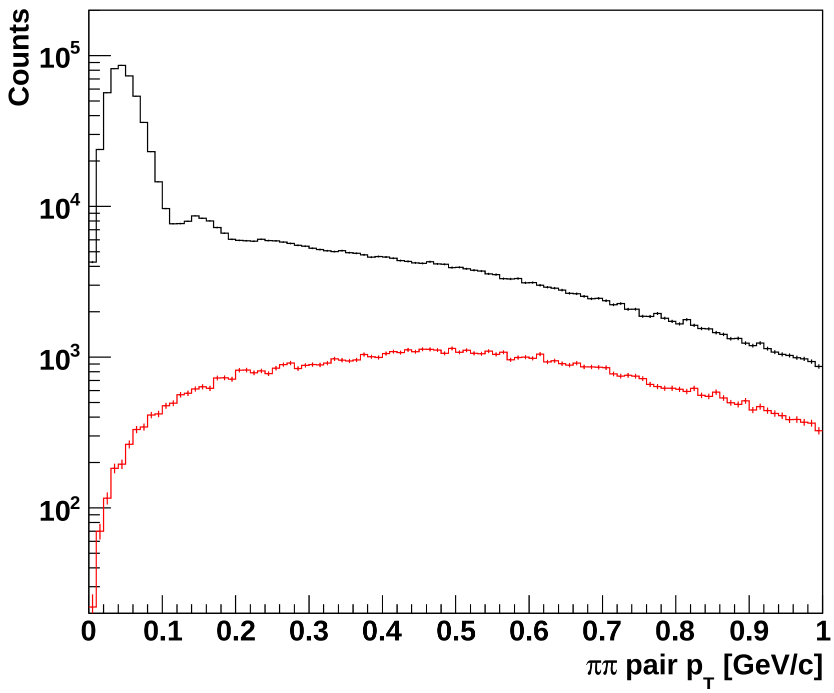

Figure 1: The black histogram shows the distribution of the pion pair transverse momentum. The peak below 100 MeV/c is from the decay of coherently produced $\pi^+\pi^-$ pairs. The red histogram shows the distribution of the pair momentum for equal sign pion pairs. Both histograms are filled with pairs that come from vertices with only two tracks.

a previous analysis [10]) to the measured incoherent $\pi^+\pi^-$ pairs. We neglect these minor backgrounds here; they are well within the overall systematic errors.

The hadronic backgrounds may be estimated from the like-sign pion pairs. Figure 1 compares the transverse momentum (p_T) of the $\pi^+\pi^-$ pair (black histogram) with the corresponding distribution for like-sign pairs (red histogram) in recorded vertices with only two tracks. The signal distribution has a prominent peak for $p_T < 100$ MeV/c. This peak is due to coherent photoproduction of pion pairs from the gold nucleus. In this region, the signal to noise ratio is very high; at larger p_T, the backgrounds are a larger fraction of the signal.

The reconstructed events are corrected for acceptance and detection efficiency using a detailed simulation of the STAR detector. A mix of ρ mesons and non-resonant $\pi\pi$ events are generated using the STARLight Monte Carlo [7] which reproduces the kinematics of the event, including the mass and p_T distributions. These events are sent through a complete GEANT simulation of the detector and then embedded in actual 'zero bias' STAR events; this embedding procedure accurately accounts for the detector noise and backgrounds, including overlapping events recorded in the STAR TPC during its sizeable active time windows. Because this single correction includes all components of the experimental setup as well as the efficiencies of the analysis algorithms, we refer to it as the “fullChain” efficiency.

A major uncertainty in the reconstruction efficiency stems from uncertainties in the actual (‘as-built’) positions of the TOF slats, which may not be completely accurately reflected in the simulations; this may affect the measured $d\sigma/dy$, particularly at large rapidity. The relative acceptance in p_T (and $t_\perp = p_T^2$) and invariant mass varies only slowly with p_T or mass, and should be insensitive to the positional uncertainties. The “fullChain” efficiency is almost independent of the pion pair p_T.

The two ZDC calorimeters detect the neutrons emitted by both beam in mutual electromagnetic dissociation with efficiency close to 100% and energy resolution sufficient to separate up to three neutron peaks. Figure 2 shows the ADC distribution from the West ZDC for events that satisfy a cut which selects events with a single neutron in the East ZDC and an exclusive and coherent photoproduced ρ^0 in the rapidity range $|y| < 1$.

This analysis considers two classes of nuclear breakup: single neutrons (1n), associated with Giant Dipole Resonance), or any number of neutrons (Xn), from a broad range of photonuclear interactions. Unfortunately, the trigger condition, requiring 1 to 4 neutrons, was incompatible with either of these classes. So, we used the 1n1n events to normalize the cross-section, based on the STARlight calculation of the cross-section. We find the ratio of triggered events to those with single neutrons in each ZDC, using the fit results in Table 1, and use the STARlight ratio of XnXn to 1n1n events to normalize the overall cross-section scale.

The relative cross-sections in Table 1 decrease slowly with increasing neutron number; for example, the cross-section for the 2n1n + 1n2n (*i.e.* the two directional combinations to get 1 neutron in one direction, 2 in the other are very similar to the 1n1n cross-section. This ratio is considerably larger than is seen for mutual Coulomb dissociation, where one calculation has the 2n1n + 1n2n : 1n1n ratio around 0.6 [23] and another finds a ratio around 0.4, albeit at a slightly lower beam energy [24]. Some of this difference is because the requirement of ρ photoproduction selects events with smaller impact parameters, where the photon spectrum is harder [18].

Figure 3 shows the efficiency-corrected, background-subtracted invariant-mass of the selected pion pairs selected to have $p_T < 100$ MeV/c. Events with dipion mass $M_{\pi\pi} > 600$ MeV/c^2 were initially fitted with a modified Söding parametrization [25] which included a relativistic Breit-Wigner resonance for the ρ^0 plus a flat direct $\pi^+\pi^-$ continuum. This 2-component model was a poor fit to the data, so an additional relativistic Breit-Wigner component was added, to account for ω photoproduction, followed by its decay to two pions $\omega \to \pi^+\pi^-$. This leads to the following fit function:

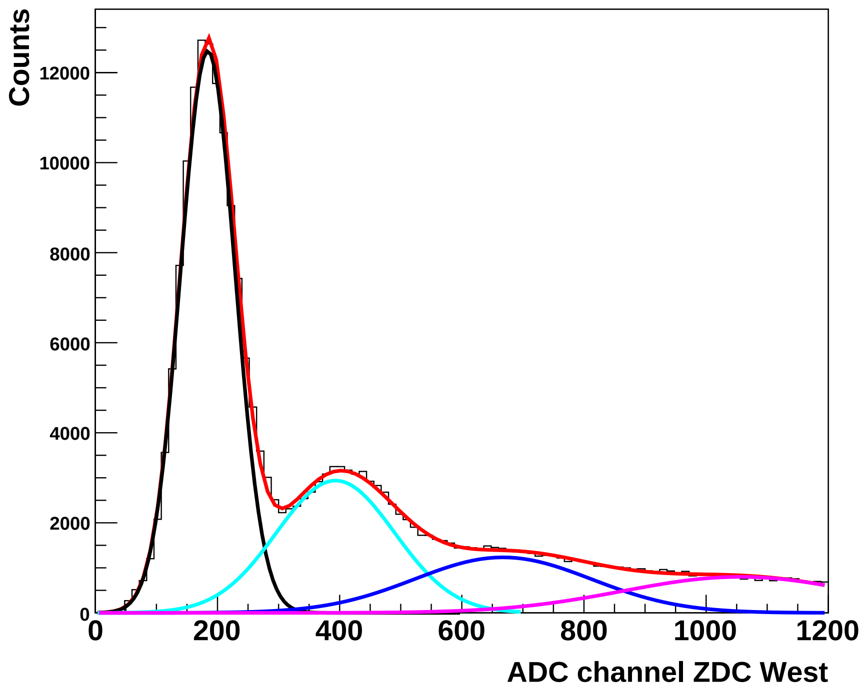

Figure 2: The shower energy in the West ZDC by neutron produced by mutual dissociation is shown as a distribution of ADC channels. These events had a single neutron detected on the East ZDC. The peaks corresponding to 1 to 4 neutrons are fitted with Gaussian distributions with standard deviations that grow as $n\sigma$ with n the number of neutrons and σ the standard deviation of the one neutron Gaussian. The red curve is the sum of all Gaussians which are also displayed individually. The quality of fit is given by $\chi^2/NDF = 498/88$ which is mostly due to the very small statistical errors.

	1n	2n	3n
1n	1.38 ± 0.24	0.57 ± 0.11	0.39 ± 0.07
2n	0.57 ± 0.11	0.23 ± 0.04	0.18 ± 0.03
3n	0.40 ± 0.07	0.19 ± 0.03	0.15 ± 0.03

Table 1: Mutual dissociation cross section (in mb) for events with exclusive coherent ρ^0 photoproduction. The row number shows the number of neutrons detected in the East ZDC and the column number lists the number of neutrons detected in the West ZDC. The cross sections listed in the table are an average of two measurements: one of them uses the West ZDC to set the number of neutrons on that beam with ADC channel cuts defined by the dip between the 1 and 2 neutron peaks, and the other measurement has the East ZDC selecting events in similar manner. These two measurements differ in the off diagonal term and the systematic uncertainty on the selection of the number of neutrons in either ZDC is set to be equal to the deviation from the average value. Statistical errors are small ($< 1\%$) and are not listed. Systematic errors arising from the cuts used to select the events added were added in quadrature to the sum in quadrature of the relevant common uncertainties listed in table 3 (17%).

$$\frac{d\sigma}{dM_{\pi^+\pi^-}} \propto \left| A_\rho \frac{\sqrt{M_{\pi\pi} M_\rho \Gamma_\rho}}{M_{\pi\pi}^2 - M_\rho^2 + iM_\rho\Gamma_\rho} + B_{\pi\pi} + C_\omega e^{i\phi_\omega} \frac{\sqrt{M_{\pi\pi} M_\omega \Gamma_\omega}}{M_{\pi\pi}^2 - M_\omega^2 + iM_\omega\Gamma_\omega} \right|^2 + f_p \tag{1}$$

where A_ρ gives the ρ component, $B_{\pi\pi}$ is for the direct pions and C_ω is for the ω. The momentum-dependent widths are taken to be

$$\Gamma_\rho = \Gamma_0 \frac{M_\rho}{M_{\pi\pi}} \left(\frac{M_{\pi\pi}^2 - 4m_\pi^2}{M_\rho^2 - 4m_\pi^2} \right)^{3/2} \tag{2}$$

and

$$\Gamma_\omega = \Gamma_0 \frac{M_\omega}{M_{\pi\pi}} \left(\frac{M_{\pi\pi}^2 - 9m_\pi^2}{M_\omega^2 - 9m_\pi^2} \right)^{3/2}, \tag{3}$$

where Γ_0 is corresponding pole width for each meson. For the ω, the $9m_\pi^2$ term is because ω decay is dominated by the three-pion channel. Here, f_p is a quadratic polynomial that describes the remaining remnant background. In this all-rapidity fit, the masses and widths of the ρ and ω were allowed to float, making for a total of ten parameters: four masses/widths, three amplitudes, and three parameters for the polynomial background.

In Fig. 3, the fitted ρ component is shown by the full blue line, with the direct $\pi\pi$ component shown in dashed black, the dashed blue line shows the interference between the two components. The full red line shows the fitted ω component and the dashed red line shows the interference between the ρ^0 and the ω components.

Table 2 shows the results of this fit. The particle masses and widths are all in quite good agreement with their generally accepted values [26]. The ω mass is considerably wider than the standard value, but it is broadened because of detector resolution; at the ω peak, the detector resolution is about 0.0085 GeV/c^2. The fit $\chi^2/DOF = 314/297$ is good.

The ω amplitude C is small, but the ω is clearly visible through its interference with the ρ. This interference produces the small kink in the spectrum just above 800 MeV/c^2. The ω amplitude agrees with a prediction based on the ω photoproduction cross-section and the most recent value for the ω branching ratio ($1.5 \pm 0.1\%$ to $\pi^+\pi^-$; this prediction is shown by the solid 'STARlight' lines in Fig. 4.

The only previous measurement of interference in the $\pi^+\pi^-$ channel is by a DESY-MIT group, using 5-7 GeV photon beams [27]. That fit used a similar, but not identical fit function, and found the $|C/A| = 0.044 \pm 0.004$ ($|C/A| = \zeta\sqrt{M_\rho\Gamma_\rho/M_\omega\Gamma_\omega}$ in their terminology).

The DESY-MIT group measured a phase angle of 1.68 ± 0.26, close to our $1.73 \pm 0.13(stat.) \pm 0.17(syst.)$. The systematic error on ϕ_ω is determined by varying the lower range of the fit to the pion pair invariant mass distribution between values of 520 and 600 MeV. This agreement is better than might be expected, since the DESY-MIT experiment used much lower energy photons, in a

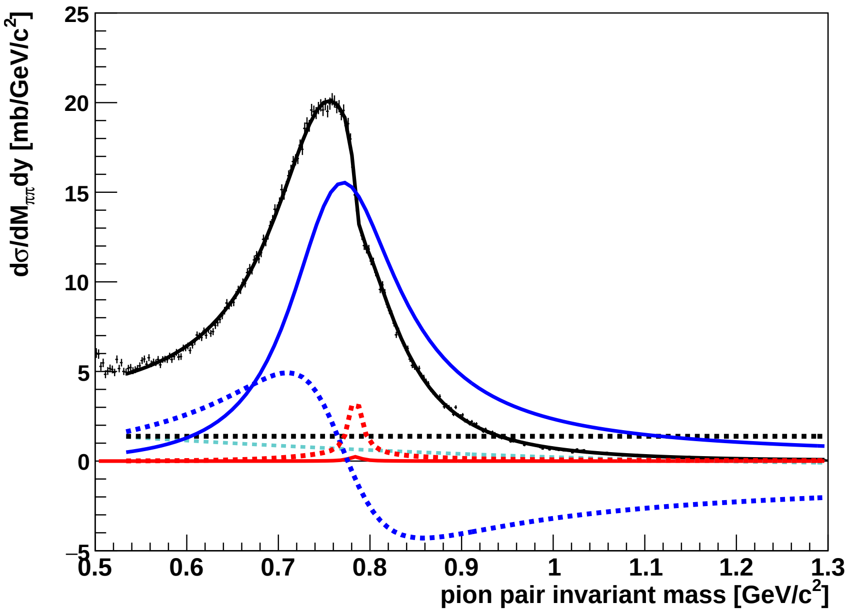

Figure 3: The $\pi^+\pi^-$ invariant-mass distribution for all selected $\pi\pi$ candidates with $p_T < 100$ MeV/c. The black markers show the data (in 2.5 MeV/c^2 bins). The black curve is the modified Söding fit to the data in the range $0.6 < M_{\pi\pi} < 1.3$ GeV. The ρ^0 Breit-Wigner component of the fitted function is shown with a blue curve and the constant non-resonant pion pair component is displayed with a black-dashed one. The interference between non-resonant pion pairs and the ρ^0 meson is shown with a blue-dashed curve and a small third order polynomial shown with a cyan-dashed curve is used to account for a remnant background. The Breit-Wigner distribution for the ω mesons is shown with a red curve and the interference between ρ^0 and ω is shown with a red-dashed curve.

Fit Parameter	value	units
M_ρ	0.7757 ± 0.0006	GeV/c^2
Γ_ρ	0.1475 ± 0.0014	GeV/c^2
A_ρ	1.511 ± 0.005	
$B_{\pi\pi}$	-1.176 ± 0.016	(GeV/c^2)$^{-1/2}$
C_ω	0.0626 ± 0.004	
M_ω	0.7838 ± 0.0009	GeV/c^2
Γ_ω	0.0163 ± 0.0017	GeV/c^2
ϕ_ω	1.73 ± 0.13	radians
$f_p\ p_0$	3.566 ± 0.304	
$f_p\ p_1$	-5.084 ± 0.53	
$f_p\ p_2$	1.743 ± 0.24	

Table 2: Parameter values extracted by fitting the invariant mass distribution of selected pion pairs with the parametrization listed in Eq. 1. Three additional parameters, giving the polynomial background, are also listed.

regime where production proceeds via both single meson and Pomeron exchange. Other experiments have studied $\rho-\omega$ interference using photoproduction to the e^+e^- final state, where the ω is more visible, but the cross sections are much smaller, or via the reaction $e^+e^- \rightarrow \pi^+\pi^-$, and gotten similar phase angles [28].

Similar fits were performed in five bins of rapidity symmetric about y=0 and variable widths. The number these bins and their widths is determined by the desire to continue to produce fits as good as the one described above. Each bin had close to 100K pion pairs and the values of M_ω and Γ_ω were fixed to the values extracted from the fit to the rapidity integrated pion pair mass distribution. Figure 4 shows the ratios $|B/A|$ and C/A at each of the five bins in rapidity. The $|B/A|$ ratio quantifies the fraction of non-resonant pion pairs in these measurements. Both $|B/A|$ and C/A are, within the total errors, flat as rapidity varies. This shows that these ratios do not have a large dependence on the photon energy.

The average value of the $|B/A|$ ratio 0.79$\pm$0.01 ($stat.$)$\pm$0.08 ($syst.$) (GeV/c^2)$^{-1/2}$ agrees, within errors, with the value reported in the previous STAR publication [10]: (0.89 ± 0.08 ($stat.$) $\pm$ 0.09 ($syst.$)). The same ratio has been measured at the higher energy of the LHC (2.76 TeV per nucleon) by the ALICE collaboration [11] which finds a smaller value (0.50 ± 0.04 ($stat.$) $+ 0.10 - 0.04$ ($syst.$)). The average $|C/A|$ value extracted from the fits in rapidity bins is 0.040 ± 0.0054 ($stat.$) $\pm$ 0.0048 ($syst.$).

Figure 5 shows the acceptance corrected distribution of ρ^0 mesons detected in events with only two tracks out of the triggered vertex The asymmetry between positive and negative rapidity gives a measure of the rapidity-dependent systematic uncertainties in the cross section. As noted above, these are likely due to asymmetries in the as-built location of the TOF counters. The magnitude of this uncertainty grows slowly from mid-rapidity to reach a value of 4% at $y = 0.7$. Since the actual lengths of the TOF system are accurately known, this uncertainty does not apply for the rapidity-integrated measurements presented

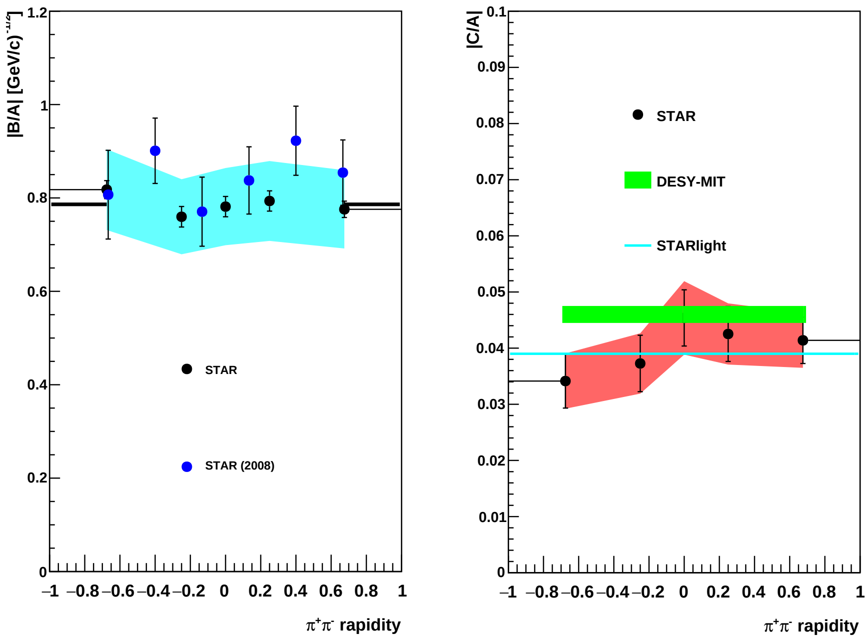

Figure 4: The left panel shows the ratio $|B/A|$ of amplitudes of non-resonant $\pi^+\pi^-$and ρ^0 mesons. The previous STAR results are shown with blue-filled circles. The right panel shows the ratio $|C/A|$ of the ω and ρ^0 amplitudes. The data is shown with red markers, while the red band includes the relevant systematic errors. The DESY-MIT $|C/A|$ measurement is shown with a green band. This measurement was at considerably lower photon energies; if converted to rapidity, these measurements would appear at large $|y$, outside the current plot. The thin cyan line shows $|C/A|$ calculated using STARlight and the most recent branching ratio for $\omega \to \pi^+\pi^-$ decay [26].

here.

Rapidity is related to photon energy k, with, at low p_T, $k = M_{\pi\pi}/2 \exp(\pm y)$, with the $\pm$ sign because of the two-fold ambiguity as to which nucleus emitted the photon, away from $y = 0$, the cross section is dominated by the lower photon energy. So, one can study how the three components of the mass fit vary with energy by dividing the mass spectrum in rapidity. We do this in five bins: $|y| < 0.15$, $0.15 < |y| < 0.35$, and $|y| > 0.35$. In each bin, fits to the corresponding invariant mass distributions were performed to separate the resonant pion pairs from the flat non-resonant distribution. The integral of the ρ Breit-Wigner function for masses ranging from $2M_\pi$ and $M_\rho + 5\Gamma_\rho$ is then used to extract a correction to the raw counts of ρ^0 candidates. This correction is then applied to all other results presented here.

Finally, the resulting distribution has been scaled by the "fullChain" efficiency defined above. The rapidity dependence of this efficiency has a bell shape with a maximum at 13% at $y \approx 0.1$. It is slightly asymmetric because of inefficiencies on one of the TPC West (rapidity < 0) sectors.

The systematic uncertainties in these measurements fall into two classes, either an overall scale factor on the cross-section, or point-to-point. The overall scale factor is usually dominant. The scaling from the rapidity distribution extracted from 1n1n events to the previously measured XnXn distribution uses a correction, extracted from the event generator STARLight and introduces a 6% uncertainty related to the uncertainty in the neutron data used as input to STARlight, squared because we detect neutrons in both beams. This uncertainty applies only to the XnXn results presented in this report. The uncertainty in the integrated luminosity is 10%, as with previous measurements [10] mainly driven by the fraction of the total Au+Au cross section accessible with the trigger used to collect this data. The selection of the number of neutrons produced in mutual electromagnetic dissociation is based on the ZDC calorimeters response. We allocate a 5% uncertainty to this neutron counting due to small non-linearities in the calorimeters and overlaps between one and many neutron distributions. We also assigned a 7% uncertainty due to modelling of the TOF system in the simulation. The track reconstruction efficiency for the STAR TPC has a 6% uncertainty [20] while the efficiency of the vertex finder is known with a 5% uncertainty driven by the effect of backgrounds. The uncertainty in how often the BBC detectors will veto good UPC events is due to fluctuating backgrounds. Even with use of embedding techniques, we estimate that these veto conditions introduce a 2% uncertainty to the results. The same-sign pion pair distributions are the best estimators for the background for these two track events. The background subtraction was done at the level of raw histograms or after a fit to the background to eliminate statistical fluctuations. The relative deviation between those two procedures found in the fully corrected distributions is found to be 1.5%. Adding all these systematic uncertainties in quadrature leads to a 19% overall common uncertainty. This uncertainty is a bit higher than in our comparable previous publication [10], largely because of additional uncertainties associated with the pileup and the more complex trigger and which is required to deal with the higher luminosities. Table 3 summarizes

Name	Value	Comment
Luminosity	10.%	
STARLight model	6.%	only for XnXn results
ZDC	5.%	ADC ch. to num. neutrons
TOF geometry modeling	7.%	
TPC tracking efficiency	6.%	STAR standard [20]
Vertex Finder efficiency	5.%	Background driven
BBC veto in trigger	2.%	Background driven
“fullChain” efficiency	7.%	Ev. Gen., Material budget
Background subtraction	1.5%	
Quadrature Sum	18.1%	

Table 3: Summary of all common systematic uncertainties identified in the generation of both the rapidity distribution shown in Fig. 5 and the -t distributions shown in figures 6 and 7. All these uncertainties are presented as a percent fractions of the measured quantities.

rapidity	PID cut	Fit to eff.	Number of track hits	TOF asymmetry
-0.70, -0.5	8.%	0.25%	0.2%	5%
-0.5, 0.	5.%	0.25%	0.05%	3.6%
0., 0.5	5.%	0.25%	0.05%	3.6%
0.5 - 0.7	8.%	0.25%	0.2%	5%

Table 4: Four point-to-point systematic uncertainties for the rapidity distribution shown in Fig. 5 shown as a percent of the measured cross section in four rapidity ranges. Pions are identified in the TPC their specific energy loss (dE/dx), based on how close (in standard deviations) they are to the calculated energy loss. Truncated distributions are used to improve accuracy [29]. Those cuts were varied simultaneously in the data and simulation to determine the systematic uncertainty due to particle identification. Good tracks are selected based on a minimum number of space points included in their pattern recognition and fits. The minimum number of hits was varied to estimate the systematic uncertainty. The rapidity distribution of photoproduced ρ^0 mesons with symmetric beams should also be a symmetric function around y=0. Relative deviations from the average between measurements at the same absolute rapidity are used to quantify the asymmetry of the measured rapidity distribution.

all the common systematic uncertainties identified in this measurement.

The main factors that introduced point-to-point systematic uncertainties in the rapidity or p_T distributions were in the track selection and particle identification. The systematic uncertainties were evaluated by varying the track quality cuts and PID cuts around their central value in both the data and simulation, and seeing how the final results varies. The largest relative deviations listed in wider bins are the point-to-point systematic uncertainties. Table 4 lists the uncertainties in the rapidity distribution. Table 5 list the point-to-point uncertainties allocated for the p_T distribution.

Recently, the ALICE collaboration has also studied ρ photoproduction, in lead-lead collisions at the Large Hadron Collider (LHC) [11]. They fit their dipion mass distribution in the range from 0.6 to 1.5 GeV^2 to a function like Eq. 1, but without the ω component, finding masses and widths consistent with the standard values. Their cross-section values, $d\sigma/dy$ were about 10% above

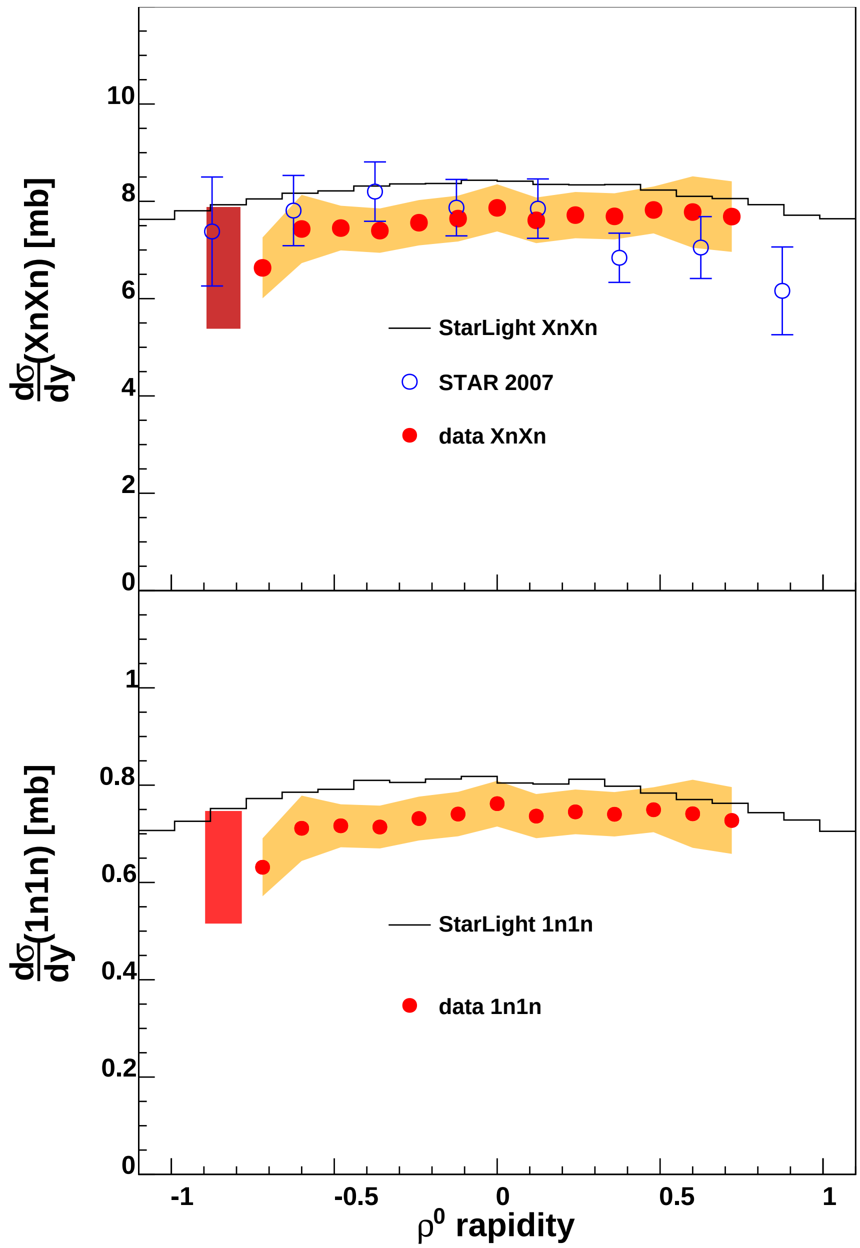

Figure 5: The cross section as function of rapidity for exclusively photo-produced ρ^0 mesons in (bottom) events with a single neutron detected on both ZDC detectors (1n1n) and for any number of neutrons XnXn (top). The data are shown with red markers. The statistical errors are smaller than the symbols, the orange band shows the quadrature sum of the point-to-point systematic uncertainties. The red box at $y \sim -0.9$ shows the quadrature sum of the common systematic uncertainties. The black histograms are the STARLight calculation for ρ^0 mesons with mutual dissociation. The blue markers in the top panel show the previous STAR measurement [10],

the STARlight

Figure 6 shows the differential cross section $d\sigma/dt$ for ρ^0 mesons after like-sign background subtraction, with t the Mandelstam variable $t = t_{\parallel} + t_{\perp}$ with $t_{\parallel} = -M_{\rho}^2/(\gamma^2 e^{\pm y})$ almost negligible and $t_{\perp} = -(p_T^{pair})^2$. The number of ρ^0 mesons is obtained from a simple scaling by a common factor of 0.75 extracted from comparisons between the number of pion pairs with invariant masses ranging from 500 MeV/c^2 to 1.5 GeV/c^2 and the integral of the ρ^0 Breit-Wigner function extracted from fits in rapidity and -t bins. In all comparisons, the integrals are performed from $2M_{\pi}$ to $M_{\rho} + 5\Gamma_{\rho}$. The yield of ρ^0 mesons is also corrected for the compounded effects of tracking reconstruction and geometrical acceptance, vertex finding efficiency and the finite track and TOF detector matching efficiency extracted from the embedded simulations. This correction is flat in t and has an average value of 6.4% over all rapidity values. Finally the distribution is normalized by the luminosity integrated over all data runs used in this analysis. The large peak in $d\sigma/dt$ for $|t| < 0.1\text{GeV}^2$ is expected from coherent photoproduction. At substantially larger $|t|$, production should be dominated by incoherent interactions with individual nucleons in the target ion.

We separate the ρ^0 t spectrum into coherent and incoherent components based on the shape of the distribution in Fig. 6. Because of the neutron requirement in the trigger, and the presence of Coulomb excitation, we cannot use the presence of neutrons from nuclear breakup as an event-by-event sign of incoherence [30].

The incoherent component is fit with the so called "dipole" form factor

$$\frac{d\sigma}{dt} = \frac{A/Q_0^2}{(1 + |t|/Q_0^2)^2}$$

used to describe low Q^2 photon-nucleon interactions [31]. The fit range for the XnXn events starts at -t = 0.2 GeV^2 (above the coherent production region) and extends to $-t = 0.45$ GeV^2 as shown by the black curve in the figure. The upper limit in t is chosen to reduce the contamination from hadronic interactions. For the events with mutual dissociation into any number of neutrons (XnXn), the fit finds $A = 3.46 \pm 0.02$, $Q_0^2 = 0.099 \pm 0.015$ (GeV/c)^2 , with $\chi^2/NDF = 19/10$. For events with mutual dissociation into single neutrons (1n1n), the fit parameters are: $A = 0.191 \pm 0.003$, $Q_0^2 = 0.099(fixed)$(GeV/c)^2, with $\chi^2/NDF = 13.7/10$. The integral of the fit to the incoherent component in the XnXn events results in a value of cross section $\sigma_{incoh} = 2.89 \pm 0.02$ $(stat.) \pm 0.03$ $(syst.)$ mb in the measured rapidity range $|y| < 1$. The integral of the coherent component discussed below amounts to 6.49 ± 0.01 $(stat.) \pm 0.01$ $(syst.)$ mb. The incoherent component of the distribution extracted from 1n1n events is fitted to the same function as the XnXn distribution. The range of -t and rapidity values is also the same. The integral of the fit to the incoherent component in the 1n1n events results in a value of cross section $\sigma_{incoh} = 0.162 \pm 0.01$ $(stat.) \pm 0.005$ $(syst.)$ mb. The integral of the 1n1n coherent component amounts to 0.7696 ± 0.004 $(stat.) \pm$ 0.004 $(syst.)$ mb.

The corresponding ratios are:

$$\sigma^{XnXn}_{incoherent}/\sigma^{XnXn}_{coherent} = 0.445 \pm 0.003(stat.) \pm 0.005(syst.)$$

$$\sigma^{1n1n}_{incoherent}/\sigma^{1n1n}_{coherent} = 0.233 \pm 0.014(stat.) \pm 0.007(syst.).$$

The difference in the ratio found for 1n1n and XnXn collision is somewhat larger than the previous STAR analysis [10], particularly in the XnXn channel. The ratio difference could come from a variety of sources. First, at large $|t|$, it is possible for a single photon to both produce a ρ^0 and leave the target nucleus excited, breaking the assumed factorization paradigm. The rate has not been calculated for ρ^0, but for J/ψ, the cross-section is substantial [32]. The calculated cross-section for vector meson production with excitation is very low for single neutron emission, so this would alter the XnXn cross-section ratio more than the 1n1n. Second, unitarity corrections could play a role here, by changing the distribution of impact parameters between 1n1n and XnXn interactions. These corrections account for the fact that, near grazing incidence, the cost of introducing another low-energy photon into the reaction is small, so four-photon reactions can occur. In these cases, one photon can excite a nucleus, for example to a a GDR, while a second photon can excite the nucleus further, leading to Xn emission rather than 1n [33].These probabilities are included in STARlight [19]. The additional photon alters the impact parameter distributions for the 1n1n and XnXn channels; the XnXn channel will experience a slightly larger reduction at small $|t|$ due to interference from the two production sites; this may lead to slightly different measured slopes and coherent/incoherent ratios. There may also be a larger effect due to a larger non-uniform photon illumination of the target nucleus.

The coherent component of the t distribution is then extracted by a subtracting the power law fit to the incoherent tail. The resulting differential cross section for ρ^0 photoproduction acompanied with mutual dissociation of the nuclei into any number of neutrons (XnXn) and only one neutron (1n1n) is shown in Fig. 7 with red and black markers respectively. In both types of events, two well defined peaks can clearly be seen. For both types of events, the location of the first dip is at $-t = 0.018 \pm 0.005$ (GeV/c)$^{-2}$. A second dip is visible at 0.043 ± 0.01 (GeV/c)$^{-2}$. An exponential function is used to characterize the spectrum below the first peak ($0.0024 < |t| < 0.0098$ (GeV/c)^2). The measured slope is 426.4 ± 1.8 (GeV/c)$^{-2}$ for the XnXn events and 407.8 ± 3.2 (GeV/c)$^{-2}$ for the 1n1n events.

Such features of the diffraction pattern indicate, to first order, the coherent diffraction off the same large target for both 1n1n and XnXn events.

At very small t, $|t| < 10^{-3}$ GeV^2, both cross section flatten out and turn downward, as can be seen in the insert in Fig. 7. This is expected due to destructive interference between ρ production on the two nuclear targets [34, 35].

The systematic uncertainties identified for the extraction of this differential cross-section come in two types, the so called common uncertaities which are the same as the ones extracted for the rapidity distribution shown in Fig. 5 and the point-to-point ones described above and listed in Table 5. The red band in

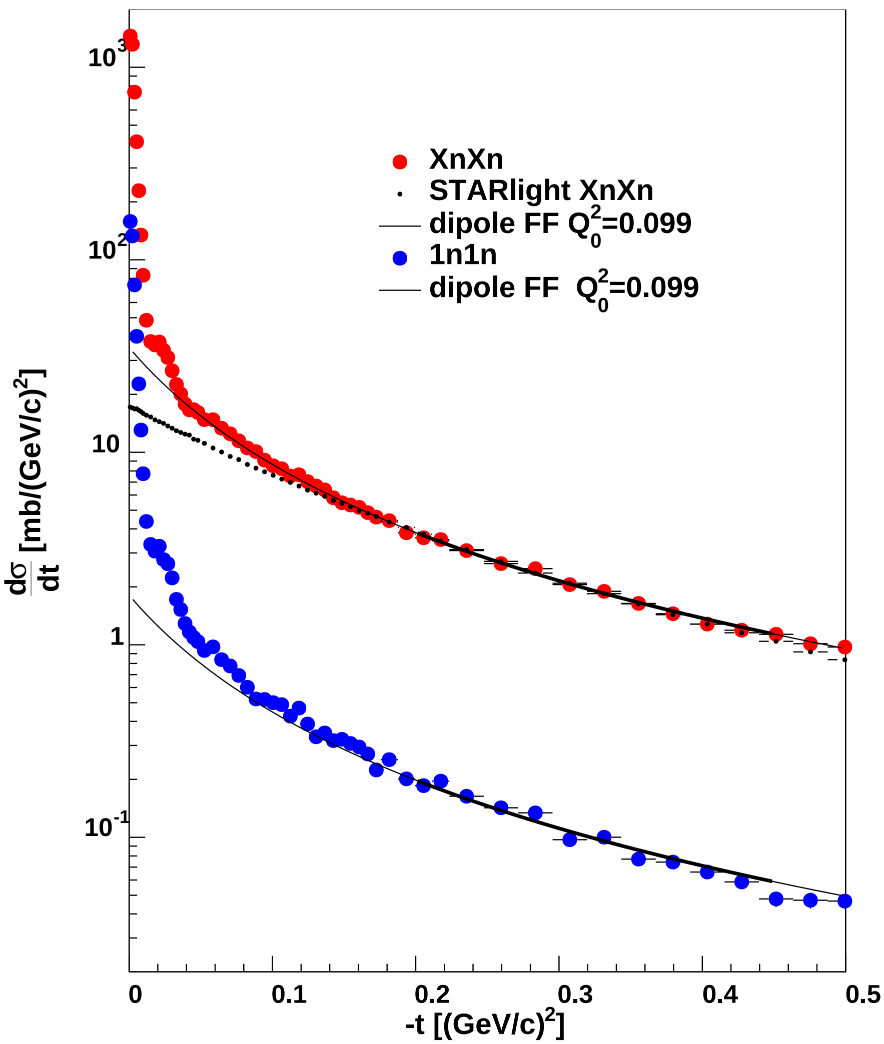

Figure 6: The final $-t$ distribution for exclusive ρ^0 mesons detected in events with mutual dissociation into a single neutron (1n1n) is shown with blue markers, the same distribution constructed from events with mutual dissociation into any number of neutrons (XnXn) is shown with red markers. The high t part of those distributions, which is dominated by the contribution from incoherent interactions is fit to a power law shape described in detail in the text. The upper limit of the fit was selected to avoid contamination from hadronic interactions, which tends to be more pronounced in the XnXn events. The fit result is shown with a solid line within the fit range and with a thinner line outside it. The incoherent component as generated by STARlight for XnXn events is shown with small black markers.

$-t[(\mathrm{GeV}/c)^2]$	track sel.	pion PID	Incoh. comp. sub.
0 - 0.02	0.2%	8%	0.5%
0.02 - 0.04	0.2%	8%	3.0%
0.04 - 0.1	0.2%	8%	8.5%

Table 5: Three point-to-point systematic uncertainties identified in the generation of the $-t$ distribution shown in Fig. 7, as a per-cent of the measured cross section in three $-t$ ranges. The PID and track selection uncertainties are described in the text. The uncertainty in the incoherent component subtraction was estimated by selecting the biggest relative deviation from the default value and cross sections extracted by changing the value of the fit parameters by one standard deviation while the other parameters remain at the default fit value.

Fig. 7 is the sum in quadrature of all systematic uncertainties as well as the statistical errors.

Similar features have been reported at the LHC in Pb + Pb at 2.76 TeV per nucleon by the ALICE collaboration [11]. They have extracted the transverse momentum distribution of the ρ^0 mesons and find a prominent coherent peak and a well defined dip around 0.12 GeV/c while this analysis finds it at $-t = 0.018 \pm 0.005$ $(\mathrm{GeV}/c)^{-2}$. The sar*t*re event generator run in UPC mode at RHIC energies [36] produces a Au nuclei recoil after ρ^0 elastic scattering with a remarkable agreement with the ρ^0 t distribution presented in this report.

The shape of $d\sigma/dt$ for coherent photoproduction is determined by the position of the interaction sites within the target, and one can, in principle, determine the density distribution of the gold nucleus via a two dimensional Fourier transform of $d\sigma/dt$. The beam energies at RHIC are high enough so that, for ρ photoproduction at mid-rapidity, the longitudinal density distribution may be neglected and the ions may be treated as discs. They are also azimuthally symmetric, so the radial distribution may be determined with a one-dimensional Fourier-Bessel (Hankel) transformation:

$$F(b) \propto \frac{1}{2\pi} \int_0^\infty dp_T p_T J_0(bp_T) \sqrt{\frac{d\sigma}{dt}} \tag{4}$$

Here, it is calculated numerically over Figure 8 shows the result of this transform, taken over the the region $|t| < 0.06$ GeV^2. The tails of the b distribution may suffer from inteference effects [35]. We varied the upper limit used in the transform in the range 0.05 to 0.09 GeV^2; this led to substantial variation at small b, shown by the cyan region in Fig. 8. The origin of this variation is not completely clear, but it may be related to aliasing due to the lack of a windowing function [37], or because of the limited statistics at large t. There is much less variation at the edges of the distribution. This leads us to believe that the transform can be used in the region where b ranges from $\sim 4 - 7$ fm. In this region, we determine the full-width half-maximum (FWHM) of the distribution to be $2 \times (6.17 \pm 0.12)$ fm. This FWHM is a measure of the hadronic size of the gold nucleus. With theoretical input, it could be compared with the electromagnetic (proton) radius of gold, as determined by electromagnetic scattering. The difference would be a measure of the neutron skin thickness of

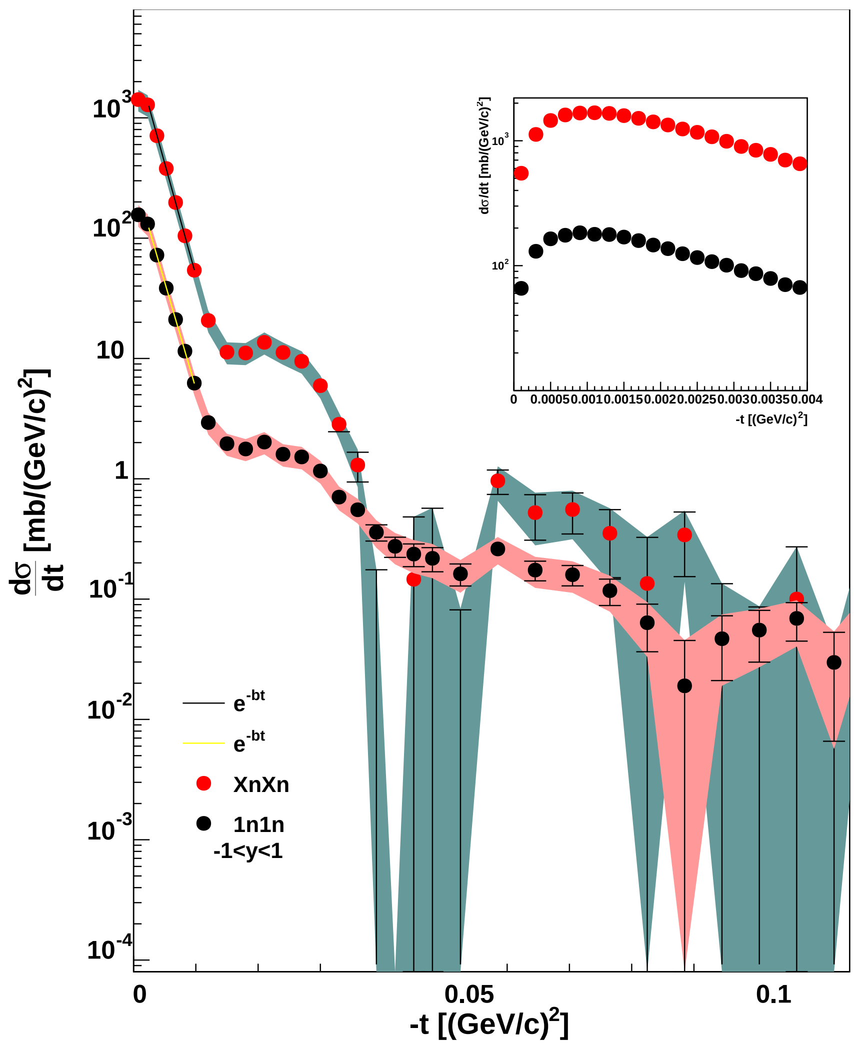

Figure 7: Fully normalized coherent diffraction patterns for ρ^0 mesons detected in exclusive XnXn events is shown with red markers. The same distribution but extracted from 1n1n events is shown with balck markers. The filled bands shows the sum in quadrature of all systematic uncertainties listed in table 4 and the statistical errors, which are shown as vertical lines.The insert shows, with finer binning at low p_T, the effects of the destructive interference between photoproduction with the photon emitted by any of the two ions.

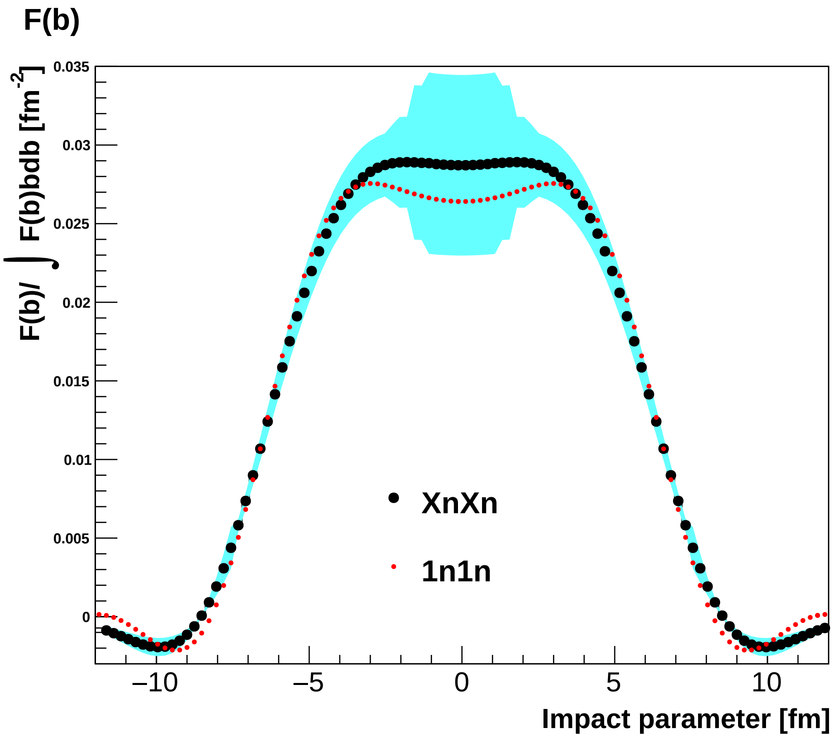

Figure 8: The histogram shows the normalized nucleon distribution in the transverse plane, the result of a two-dimensional Fourier transfom (Hankel transform) of the XnXn and 1n1n diffraction patterns shown in Fig. 7. The integration is limited to a region where data is available; in the range $0 < |t| < 0.06$ GeV^2. The cyan error band shows the effect of changing the maximum t to 0.05, 0.07 and 0.09 GeV^2. In order to highlight the similarity of both results at their falling edges, the resulting histograms are scaled by their integrals from -12 to 12 fm. The FWHM of both transforms is $2 \times (6.17 \pm 0.12)$ fm consistent with the coherent diffraction of ρ^0 mesons off an object as big as the Au nuclei.

gold, something that is difficult to measure [38], [39].

Because of the possibility of ρ absorption the p_T introduced by the photon, the non-uniformity of the photon field (it is stronger on the 'near' side of the nucleus) and the effect of interference between the two production sites, corrections are required, and care must be used in interpreting the transform.

3. Summary and conclusion

In conclusion, STAR has made a high-precision study of ρ, ω and direct $\pi^+\pi^-$ photoproduction in 200 GeV/nucleon gold-on-gold ultra-peripheral collisions, using 394,000 $\pi^+\pi^-$ pairs. We measure the cross section $d\sigma/dt$ over a wide range. The incoherent cross section has a very similar shape to the HERA data on $\gamma p \to \rho^0 p$, while the coherent contribution can be used to map out the density distribution of the gold target nuclei. We also fit the invariant mass spectrum to a mixture of ρ, ω and direct $\pi^+\pi^-$ (including interference terms). The ratio of ρ to direct $\pi\pi$ is similar to that in previous measurements, while the newly measured ω contribution is comparable with predictions based on on the previously measured $\gamma p \rightarrow \omega p$ cross section and the $\omega \rightarrow \pi^+\pi^-$ branching ratio. The relative fractions of ρ, ω and direct $\pi^+\pi^-$ do not vary significantly with rapidity, indicating that they all have a similar dependence on photon energy.

This measurement provides a nice lead-in to future studies of photo- and electro- production at an electron-ion collider (EIC) [40], where nuclei may be probed with photons at a wide range of Q^2 [41].

4. Acknowledgments

References

[1] G. Baur, K. Hencken, D. Trautmann, S. Sadovsky, Y. Kharlov, Coherent gamma gamma and gamma-A interactions in very peripheral collisions at relativistic ion colliders, Phys.Rept. 364 (2002) 359–450. `arXiv:hep-ph/0112211`, `doi:10.1016/S0370-1573(01)00101-6`.

[2] C. A. Bertulani, S. R. Klein, J. Nystrand, Physics of ultra-peripheral nuclear collisions, Ann. Rev. Nucl. Part. Sci. 55 (2005) 271–310. `arXiv:nucl-ex/0502005`, `doi:10.1146/annurev.nucl.55.090704.151526`.

[3] J. Crittenden, Exclusive production of neutral vector mesons at the electron - proton collider HERA`arXiv:hep-ex/9704009`.

[4] S. Nussinov, Colored-quark version of some hadronic puzzles, Phys. Rev. Lett. 34 (1975) 1286–1289. `doi:10.1103/PhysRevLett.34.1286`.
URL `http://link.aps.org/doi/10.1103/PhysRevLett.34.1286`

[5] F. E. Low, Model of the bare pomeron, Phys. Rev. D 12 (1975) 163–173. `doi:10.1103/PhysRevD.12.163`.
URL `http://link.aps.org/doi/10.1103/PhysRevD.12.163`

[6] J. Bartels, K. J. Golec-Biernat, H. Kowalski, A modification of the saturation model: DGLAP evolution, Phys.Rev. D66 (2002) 014001. `arXiv:hep-ph/0203258`, `doi:10.1103/PhysRevD.66.014001`.

[7] S. R. Klein, J. Nystrand, Exclusive vector meson production in relativistic heavy ion collisions, Phys. Rev. C 60 (1999) 014903. `doi:10.1103/PhysRevC.60.014903`.
URL `http://link.aps.org/doi/10.1103/PhysRevC.60.014903`

[8] G. Agakishiev, et al., ρ^0 Photoproduction in AuAu Collisions at $\sqrt{s_{NN}}$=62.4 GeV with STAR, Phys. Rev. C85 (2012) 014910. `arXiv:1107.4630`, `doi:10.1103/PhysRevC.85.014910`.

[9] C. Adler, et al., Coherent rho^0 production in ultraperipheral heavy ion collisions, Phys. Rev. Lett. 89 (2002) 272302. arXiv:nucl-ex/0206004, doi:10.1103/PhysRevLett.89.272302.

[10] B. I. Abelev, et al., ρ^0 Photoproduction in Ultra-Peripheral Relativistic Heavy Ion Collisions with STAR, Phys. Rev. C77 (2008) 034910. arXiv:0712.3320, doi:10.1103/PhysRevC.77.034910.

[11] J. Adam, et al., Coherent ρ^0 photoproduction in ultra-peripheral Pb–Pb collisions at $\sqrt{s_{\rm NN}} = 2.76$ TeVarXiv:1503.09177.

[12] L. Frankfurt, M. Strikman, M. Zhalov, Predictions of the generalized Glauber model for the coherent rho production at RHIC and the STAR data, Phys. Rev. C67 (2003) 034901. arXiv:hep-ph/0210303, doi:10.1103/PhysRevC.67.034901.

[13] L. Frankfurt, V. Guzey, M. Strikman, M. Zhalov, Nuclear shadowing in photoproduction of ρ mesons in ultraperipheral nucleus collisions at RHIC and the LHCarXiv:1506.07150.

[14] V. P. Goncalves, M. V. T. Machado, Photoproduction of ρ^0 meson in ultra-peripheral heavy ion collisions at the BNL RHIC and CERN LHC, Phys. Rev. C80 (2009) 054901. arXiv:0907.4123, doi:10.1103/PhysRevC.80.054901.

[15] G. Sampaio dos Santos, M. V. T. Machado, Light vector meson photoproduction in hadron-hadron and nucleus-nucleus collisions at energies available at the CERN Large Hadron Collider, Phys. Rev. C91 (2) (2015) 025203. arXiv:1407.4148, doi:10.1103/PhysRevC.91.025203.

[16] M. Klusek-Gawenda, A. Szczurek, $\pi^+\pi^-$ and $\pi^0\pi^0$ pair production in photon-photon and in ultraperipheral ultrarelativistic heavy ion collisions, Phys. Rev. C87 (5) (2013) 054908. arXiv:1302.4204, doi:10.1103/PhysRevC.87.054908.

[17] B. L. Berman, S. C. Fultz, Measurements of the giant dipole resonance with monoenergetic photons, Rev. Mod. Phys. 47 (1975) 713–761. doi:10.1103/RevModPhys.47.713.
URL http://link.aps.org/doi/10.1103/RevModPhys.47.713

[18] G. Baur, K. Hencken, A. Aste, D. Trautmann, S. R. Klein, Multiphoton exchange processes in ultraperipheral relativistic heavy ion collisions, Nucl. Phys. A729 (2003) 787–808. arXiv:nucl-th/0307031, doi:10.1016/j.nuclphysa.2003.09.006.

[19] A. J. Baltz, S. R. Klein, J. Nystrand, Coherent vector meson photoproduction with nuclear breakup in relativistic heavy ion collisions, Phys. Rev. Lett. 89 (2002) 012301. arXiv:nucl-th/0205031, doi:10.1103/PhysRevLett.89.012301.

[20] M. Anderson, et al., The Star time projection chamber: A Unique tool for studying high multiplicity events at RHIC, Nucl.Instrum.Meth. A499 (2003) 659–678. arXiv:nucl-ex/0301015, doi:10.1016/S0168-9002(02)01964-2.

[21] W. J. Llope, The large-area time-of-flight upgrade for STAR, Nucl. Instrum. Meth. B241 (2005) 306–310. doi:10.1016/j.nimb.2005.07.089.

[22] C. Adler, A. Denisov, E. Garcia, M. Murray, H. Strobele, S. White, The RHIC zero-degree calorimeters, Nucl. Instrum. Meth. A499 (2003) 433–436. doi:10.1016/j.nima.2003.08.112.

[23] I. A. Pshenichnov, J. P. Bondorf, I. N. Mishustin, A. Ventura, S. Masetti, Mutual heavy ion dissociation in peripheral collisions at ultrarelativistic energies, Phys. Rev. C64 (2001) 024903. arXiv:nucl-th/0101035, doi:10.1103/PhysRevC.64.024903.

[24] M. Klusek-Gawenda, M. Ciemala, W. Schafer, A. Szczurek, Electromagnetic excitation of nuclei and neutron evaporation in ultrarelativistic ultraperipheral heavy ion collisions, Phys. Rev. C89 (5) (2014) 054907. arXiv:1311.1938, doi:10.1103/PhysRevC.89.054907.

[25] P. Soding, On the Apparent shift of the rho meson mass in photoproduction, Phys. Lett. 19 (1966) 702–704. doi:10.1016/0031-9163(66)90451-3.

[26] K. A. Olive, et al., Review of Particle Physics, Chin. Phys. C38 (2014) 090001. doi:10.1088/1674-1137/38/9/090001.

[27] H. Alvensleben, et al., Precise determination of rho-omega interference parameters from photoproduction of vector mesons off nucleon and nuclei, Phys. Rev. Lett. 27 (1971) 888–892. doi:10.1103/PhysRevLett.27.888.

[28] P. Langacker, Quark Mass Differences and $\rho - \omega$ Mixing, Phys. Rev. D20 (1979) 2983. doi:10.1103/PhysRevD.20.2983.

[29] Y. Xu, O. Barannikova, H. Bichsel, X. Dong, P. Fachini, Y. Fisyak, A. Kocoloski, B. Mohanty, P. Netrakanti, L. Ruan, M. C. Suarez, Z. Tang, G. van Buren, Z. Xu, Nuclear Instruments and Methods in Physics Research Section A: Accelerators, Spectrometers, Detectors and Associated Equipment 614 (1) (2010) 28 – 33. doi:http://dx.doi.org/10.1016/j.nima.2009.12.011, [link]. URL http://www.sciencedirect.com/science/article/pii/S0168900209023067

[30] V. Rebyakova, M. Strikman, M. Zhalov, Coherent ρ and J/ψ photoproduction in ultraperipheral processes with electromagnetic dissociation of heavy ions at RHIC and LHC, Phys. Lett. B710 (2012) 647–653. arXiv:1109.0737, doi:10.1016/j.physletb.2012.03.041.

[31] M. Drees, D. Zeppenfeld, Production of supersymmetric particles in elastic *ep* collisions, Phys. Rev. D 39 (1989) 2536–2546. doi:10.1103/PhysRevD.39.2536.
URL http://link.aps.org/doi/10.1103/PhysRevD.39.2536

[32] M. Strikman, M. Tverskoy, M. Zhalov, Neutron tagging of quasielastic J/psi photoproduction off nucleus in ultraperipheral heavy ion collisions at RHIC energies, Phys. Lett. B626 (2005) 72–79. arXiv:hep-ph/0505023, doi:10.1016/j.physletb.2005.08.083.

[33] A. J. Baltz, M. J. Rhoades-Brown, J. Weneser, Heavy ion partial beam lifetimes due to Coulomb induced processes, Phys. Rev. E54 (1996) 4233–4239. doi:10.1103/PhysRevE.54.4233.

[34] S. R. Klein, J. Nystrand, Interference in exclusive vector meson production in heavy ion collisions, Phys. Rev. Lett. 84 (2000) 2330–2333. arXiv:hep-ph/9909237, doi:10.1103/PhysRevLett.84.2330.

[35] B. I. Abelev, et al., Observation of Two-source Interference in the Photoproduction Reaction Au Au —¿ Au Au ρ^0, Phys. Rev. Lett. 102 (2009) 112301. arXiv:0812.1063, doi:10.1103/PhysRevLett.102.112301.

[36] T. Toll, T. Ullrich, The dipole model Monte Carlo generator Sartre 1, Comput.Phys.Commun. 185 (2014) 1835–1853. arXiv:1307.8059, doi:10.1016/j.cpc.2014.03.010.

[37] Window Function.
URL https://en.wikipedia.org/wiki/Window_function

[38] C. M. Tarbert, et al., Neutron skin of ^{208}Pb from Coherent Pion Photoproduction, Phys. Rev. Lett. 112 (24) (2014) 242502. arXiv:1311.0168, doi:10.1103/PhysRevLett.112.242502.

[39] A. Gardestig, C. J. Horowitz, G. A. Miller, Comment on "Neutron Skin of ^{208}Pb from Coherent Pion Photoproduction"arXiv:1504.08347.

[40] A. Accardi, et al., Electron Ion Collider: The Next QCD Frontier - Understanding the glue that binds us allarXiv:1212.1701.

[41] T. Toll, T. Ullrich, Exclusive diffractive processes in electron-ion collisions, Phys.Rev. C87 (2) (2013) 024913. arXiv:1211.3048, doi:10.1103/PhysRevC.87.024913.